Effect of SiC addition on processability of AISI S2 tool steel for laser powder bed fusion

SAGGIONETTO Enrico[1,a], ROGER VILA Gerard[1,b], DEDRY Olivier[1,c],
TCHOUFANG TCHUINDJANG Jérôme[1,d] and MERTENS Anne[1,e,*]

[1]Metallic Materials Science (MMS) team, Aerospace and Mechanical Engineering Dpt.,
University of Liège, Belgium

[a]enrico.saggionetto@uliege.be, [b]gerard.rogervila@student.uliege.be, [c]olivier.dedry@uliege.be,
[d]j.tchuindjang@uliege.be, [e]anne.mertens@uliege.be

Keywords: Additive Manufacturing, Laser Powder Bed Fusion, Tool Steel, Melt Pool

Abstract. Laser Powder Bed Fusion (LPBF) of metallic alloys allows to achieve complex shape parts with innovative properties. However, the commercial availability of powder for LPBF is still limited, thus restraining the development of new alloys. To overcome this shortcoming, mixing different powders allows to tailor the chemical composition, although affecting the LPBF process. Indeed, to achieve a fully dense and defect-free part a proper melt pool must be generated during the LPBF process, in order to ensure good overlapping between each track and layer. Melt pools can be described as conductive or key-hole like, promoting the appearance of process-induced defects such as lack of fusion or key-hole porosities. Processing a mixture of several powders by changing the amount of one constituent can affect the type of melt pool generated during the process, thus shifting the process map. In this work, AISI S2 tool steel powders are enriched with 5 and 10% (in volume) of Silicon Carbide (SiC) and processed by LPBF. The effect of SiC on the processability is discussed for different volumetric energy density (E_d). Defects within cross sections are characterized and quantified, as well as the melt pool depth and morphology.

Introduction

Over recent years, the development of new metallic alloys manufactured by Laser Powder Bed Fusion (LPBF) has been the object of increasing attention. Indeed, the ultra-fast heating and cooling rates involved during the LPBF process are responsible for the formation of strongly out-of-equilibrium microstructures, involving supersaturated solid solution as well as new metastable phases, thus offering new possibilities in terms of usage properties such as mechanical, corrosion and tribological properties. However, these conditions make difficult the processing of metal alloys such as high carbon tool steels, due to the tendency to the formation of cracks that makes the final part unusable [1]. On the other hand, the use of LPBF allows to produce complex shape parts implementing internal cooling channels, difficult to obtain by conventional manufacturing methods. Therefore, research is now focusing on the development by LPBF of tool steels with complex chemical composition in order to combine all the advantages of this technology.

However, the commercial availability of metal powders suitable for LPBF is still limited. Therefore, the processability of new metal alloys with specific chemical composition is restrained. One way to overcome this hurdle is the mixing of different powders to tailor the composition. Obtaining a proper powder mixture is often challenging because of the dependence of the processability on the rheological properties of the mixture, such as spreadability and packability [2]. To achieve a fully dense, defect-free part, proper melt pools must be generated during the LPBF process, in order to ensure good overlapping between each track and layer [3]. Melt pool quality can lead to the presence of defects and porosities such as lack of fusion, key-hole, balling and spattering. Melt pools are classified as conductive or key-hole [4]. A conductive melt pool is usually shallow, resulting in insufficient liquid phase for the powders to bond together and thus

generating lack of fusion defects. On the contrary, unstable key-hole melt pools are responsible for the formation of key-hole porosities, due to excessive evaporation that causes entrapment of gas at the bottom of the melt pool. The type of melt pool is affected by the processing parameters, such as laser power, scan speed, layer thickness and hatch distance. Such parameters are encased within the volumetric energy density E_d. Usually, low E_d as result of low power and high scan velocity leads to a conductive shallow melt pool. In contrast, high E_d as result of high power and low scan velocity leads to the formation of unstable key-hole melt pools. The transition from conductive to key-hole is accompanied by a change in the morphology of the melt pool from semi-circular to key-hole like [5]. Close to the threshold for transition, stable key-hole melt pool generated by intermediate parameters allows to achieve defect-free parts.

Understanding the proper process parameters to ensure an optimal melt pool is crucial for the processability of new metal alloys for LPBF. The above-mentioned types of melt pool are affected by the interaction of the laser with both powder and solidified material underneath the powder layer. Indeed, properties such as absorption of the laser energy on powders, thermal conductivity of both powder and solidified material play a crucial role on the melt pool generated [6–9]. These properties depend on powder characteristics such as particle size distribution, morphology, roughness etc. The complexity of such phenomena increases when a mixture of different powders is processed. Different works reported the change in powder absorptivity when nanoparticles are added to the mixture, as well as a change in the temperature of melt pool due to a change in conductivity [5,10–13]. Therefore, the processing of different powder mixtures can change the melt pool features, thus affecting the processability of the material.

This work focuses in particular on the effect of SiC on the processability of the low alloy tool steel AISI S2, previously processed as reference material [14]. A restriction of the process map is observed with increasing amount of SiC, due to a change in the type and depth of melt pools generated during the process.

Materials and methods

Commercial gas atomized powders AISI S2 Tool Steel (0.49 C, 1.2 Si, 0.6 Mo, 0.6 Mn, Fe bal., wt. %) and Silicon Carbide (SiC) were used as raw material. The particle size distribution of the SiC powder is given as follows: D10 = 0.4 µm, D50 = 0.75 µm and D90 = 1.5 µm. More details concerning the AISI S2 tool steel powder may be found in our previous work [14]. SiC powder was added in 5 and 10% (in volume) to S2 tool steel powder.

Starting from the powders, cubes of $10x10x10$ mm^3 were produced with an Aconity3D Mini LPBF machine under argon atmosphere. A fixed power (P) of 200 W was combined with a scan velocity (v_s) from 500 to 2000 mm/s (Table 1). A laser spot size of 80 µm with a gaussian distribution, a layer thickness (t) of 30 µm and a hatch spacing (h) of 80 µm were used for all samples. The scanning strategy implied a rotation of 90° for each layer, with no contouring. No preheating of the substrate was applied. More details about the processing parameters can be found in our previous work [14].

The volumetric energy density (E_d) was used to correlate the results observed with the processing parameters (Eq. 1).

$$E_d = \frac{P}{t*h*v_s}. \tag{1}$$

Table 1 lists the samples studied in this work, together with their processing parameters. The codification of each sample considers the powder mixture used (0, 5, 10 for the mixture S2, S2 + 5% SiC, S2 + 10% SiC respectively) followed by the level of E_d (1, 2, 3, 4). E_d is classified based on the intensity from low to high, with numbers from 1 to 4 corresponding to an approximative value of E_d of 40, 80, 115, 170 J/mm^3 respectively. Sample 10.1 was not fully processed, as the

printing was stopped after few layers due to the appearance of an irregular surface. Therefore, sample 10.1 was not considered for further analysis.

Tab. 1. Processing parameters and volumetric energy density (Ed) for each sample.

Powder mixture	Sample	P [W]	v_s [mm/s]	E_d [J/mm^3]
S2	0.1	200	2000	42
	0.2	200	1000	83
	0.3	200	750	111
	0.4	200	500	167
S2 + 5% SiC	5.1	200	2000	42
	5.2	200	1000	83
	5.3	200	750	111
	5.4	200	500	167
S2 + 10% SiC	10.1	200	2000	42
	10.2	200	1000	83
	10.3	200	700	119
	10.4	200	500	167

All as-built samples were cut by Electro Discharge Machining perpendicularly to the laser scan direction of the last layer to obtain the cross section. After cutting, samples were hot mounted with an electrically conductive Bakelite, then ground and polished down to 1 μm. Defects within the cross sections as well as melt pool dimensions were analyzed through an optical microscope Olympus BX60. Nital 3% was used to etch the cross sections.

Results

Fig. 1 shows an overview of the cross section of each sample, where the main defects present are highlighted and quantified through the percentage of porosity ε. Samples obtained with S2 powder exhibits lack of fusion defects for low E_d (sample 0.1) and key-hole porosities for high E_d (sample 0.4). At the intermediates values of E_d of 80 and 115 J/mm^3 (sample 0.2, 0.3) only small gas porosities are spotted. With the addition of SiC, the amount of lack of fusion defects significantly increases for low E_d of 40 J/mm^3, passing from being 1.4% in sample 0.1 to 19% in sample 5.1. Similarly, for E_d of 80 J/mm^3, sample 0.2 has 0.04% porosity, being mainly small gas porosities, whereas sample 5.2 has 0.2% porosity, associated to lack of fusion defects. The amount of porosity further increases up to 1% in sample 10.2. For E_d of 115 J/mm^3 only small gas porosities are spotted in all samples. At the highest value of E_d, key-hole porosities are visible in all samples (0.4, 5.4, 10.4), with an amount remaining within the same order of magnitude between 0.4 – 0.7%. It is important to mention that with 10% SiC all samples exhibited cracks.
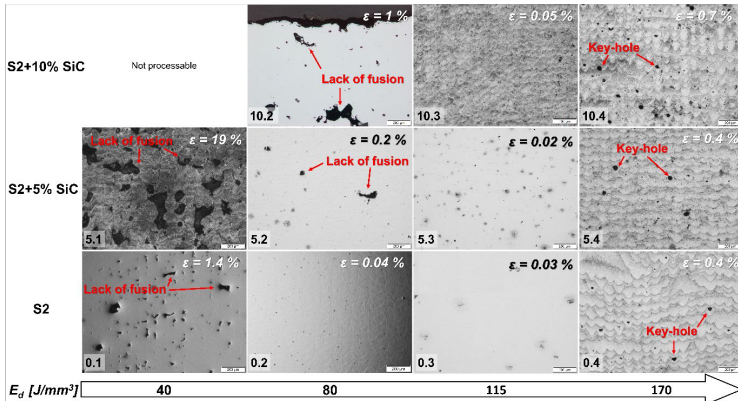
Fig. 1. Cross section overviews of each sample, varying the amount of SiC and E_d. Defects are highlighted in terms of type (lack of fusion or key-hole) and amount (percentage of porosity ε). Samples 0.3, 5.2 and 5.3 exhibits imperfections due to the polishing conditions.

Fig. 2 shows an overview of the top layer of each sample, where melt pools are highlighted. Shallow melt pools are visible at the lowest value of E_d, with a semi-circular shape and poor overlapping between each track. The irregularity of each track and layer increases passing from sample 0.1 to 5.1. Increasing E_d, in the range $80 – 170$ J/mm^3 the melt pool morphology changes to key-hole like, except for sample 10.2 where the melt pool morphology is still semi-circular. Key-hole defects are visible at the bottom of the melt pool of samples 0.4, 5.4, 10.4 generated at the highest E_d of 170 J/mm^3.
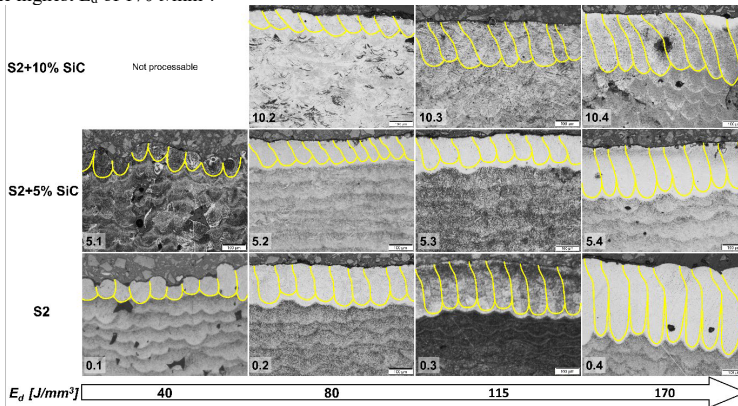

Fig. 2. Top layer overviews of each sample, varying the amount of SiC and E_d. Melt pools morphologies are highlighted.

Fig. 3 shows the melt pool depth of each sample. In general, the depth clearly increases as E_d increases. Furthermore, the addition of SiC leads to a decrease in melt pool depth for all E_d. For E_d of 40 J/mm^3, the depth is similar for S2 and S2 + 5% SiC, being around 100 µm. Similarly, for E_d of 80 J/mm^3 the depth is between 90 – 120 µm with 5 and 10% SiC, increasing up to 190 µm for S2. For E_d of 115 J/mm^3, the melt pool depth is within the range 150 – 250 µm. Finally, for E_d of 170 J/mm^3, all the melt pool depths are higher than 250 µm, with S2 reaching a value close to 350 µm.
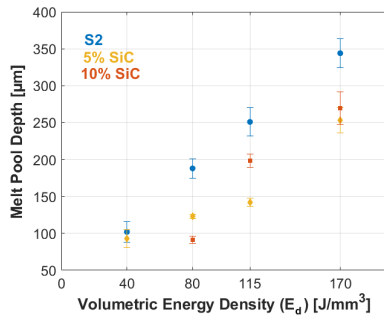

Fig. 3. Melt pool depths changes varying the amount of SiC and E_d.

Discussion

The nature of the melt pools generated during the LPBF process is responsible for the achievement of a sound part, fully dense and defect-free or, on the contrary, for the appearance of defects such as lack of fusion or key-hole porosities. According to equation 1, E_d depends on four different parameters: laser power, laser scan velocity, layer thickness and hatch distance. The type of melt pool generated depends on the final value of E_d as well as on the individual value of each single parameter. To consider this aspect, in this work, different values of E_d are investigated as a result of the change of the laser scan velocity as the only parameter that is varied. Laser power, layer thickness and hatch distance are fixed. Furthermore, samples obtained by processing the mixture of S2 + 10% (in vol.) SiC exhibited cracks at all E_d. Nevertheless, these samples are still considered in this work for a more comprehensive investigation on the effect of SiC addition on the processability of S2 tool steel powder.

Fig. 2 shows the melt pool formed depending on the initial amount of SiC and on the applied E_d. A semi-circular shape with a depth close to 100 µm (Fig. 3) is observed for low E_d of 40 J/mm^3. Such morphology is associated with a conductive melt pool type, which leads to the appearance of lack of fusion defects. Indeed, the melt pool generated is not sufficient to melt a significant amount of powders. Only a limited re-melting of the underneath material occurs, thus creating poor overlapping between each track and layer. Despite the similar depth of melt pools of samples 0.1 and 5.1 (Fig. 3), the addition of 5% SiC leads to the generation of more irregular melt pools in sample 5.1 compared to sample 0.1 (Fig. 2), worsening the overlapping and the quality of each track and layer with the advancement of the process. Thus, there is a significant increase in the amount of porosity ε, from 1.4 up to 19% when passing from 0 to 5% SiC respectively (Fig. 1). With 10% SiC, the printing of sample 10.1 was interrupted due to the appearance of an irregular surface. It can be assumed that, in this case, the melt pool formed is shallow and conductive,

leading to bad overlapping between each track causing irregular layers that finally affect the surface quality.

Increasing E_d up to 80 J/mm^3 leads to the appearance of a stable key-hole melt pool for samples 0.2 and 5.2. However, sample 0.2 alone does not exhibit any defect (Fig. 1). With the addition of 5% SiC, few lack of fusion defects are still present in sample 5.2 (Fig. 1), due to the generation of a shallow melt pool that leads to poor overlapping (Fig. 2). Indeed, despite a stable key-hole morphology, the depth of the melt pool is around 120 µm (Fig. 3), which remains close to the melt pool depth at 40 J/mm^3 (100 µm). In contrast, sample 0.2 exhibits a deeper melt pool around 200 µm, which allows for good overlapping between each track and layer. With 10% SiC (sample 10.2), the melt pool has still a conductive morphology (Fig. 2) with a depth of 90 µm (Fig. 3). Thus, as in the case of an E_d of 40 J/mm^3, lack of fusion defects are present.

At 115 J/mm^3, for all compositions a stable key-hole melt pool is generated, avoiding the presence of defects. Only few little gas porosities are spotted. The depth of the melt pool is between 150 and 250 µm.

Finally, for the highest E_d of 170 J/mm^3, an unstable key-hole melt pool is visible for all compositions, leading to presence of key-hole defects at the bottom of the melt pool (Fig. 1 and Fig. 2). Such defects are present in similar amounts for all compositions, i.e. less than 1%.

For all the processed powder mixtures, a sound part free of process-induced defects such as lack of fusion or key-hole porosities is obtained when the melt pool exhibits a stable key-hole like morphology with a depth between 150 and 250 µm. The threshold for the change from conductive to stable key-hole melt pool is observed to be of E_d of 80 J/mm^3 for the powder mixtures S2 and S2 + 5% SiC. However, with the addition of 5% SiC, a proper stable key-hole melt pool with sufficient depth is only generated at 115 J/mm^3, which remains appropriate for S2 powder alone. With 10% SiC, the threshold for the change from conductive to stable key-hole melt pool is shifted to E_d of 115 J/mm^3. When further increasing E_d up to 170 J/mm^3, an unstable key-hole melt pool is generated for all compositions. Therefore, the addition of SiC restrains the optimal process window to obtain a sound part. Such restriction of the optimal process window may be ascribed to powder properties such as particle size distribution, laser energy absorptivity and reflection as well as packing density and conductivity of both the powders and solidified material. Further investigations are being conducted to gain a deeper understanding of these phenomena. Fig. 4 shows a schematic representation of the melt pool types and corresponding defects with varying E_d and SiC additions.
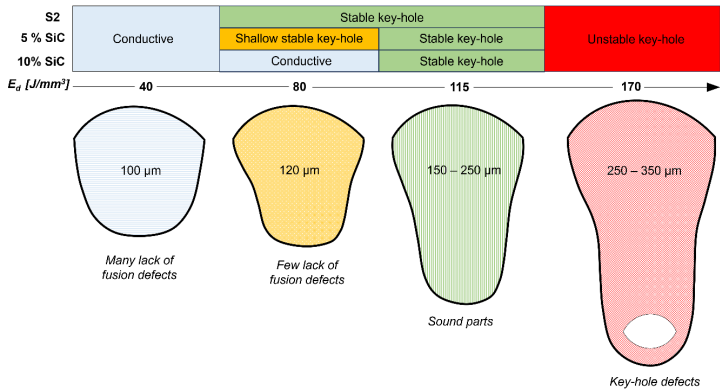
Fig. 4. Schematic representation of the types of melt pool generated during the LPBF process with varying E_d and SiC additions. A stable key-hole like melt pool with a depth between 150 and 250 µm is desired to obtain a sound part. For S2 parts, such melt pool is obtained for E_d between 80 and 115 J/mm³, being limited to 115 J/mm³ when 5 and 10% SiC is added.

Summary and conclusions

- SiC powder was added in proportion of 5 and 10 % (in volume) to a tool steel AISI S2 powder and processed by LPBF. Processing parameters were varied using different scan velocity, keeping a fixed laser power, layer thickness and hatch distance. Four values of E_d were considered (40, 80, 115, 170 J/mm³) for investigations.

- For AISI S2 samples, lack of fusion defects are present only for the lowest E_d (40 J/mm³). When adding SiC in proportion of either 5 and 10% in volume, such defects are present even for E_d of 80 J/mm³.

- The restriction of the optimal process window can be linked to a change in melt pool morphology and dimensions. Conductive melt pools are present for the lowest E_d of 40 J/mm³ causing lack of fusion defects for S2 and S2 + 5% SiC. With S2 + 10% SiC, a conductive melt pool is still present for E_d of 80 J/mm³. Unstable key-hole like melt pools are present at the highest E_d of 170 J/mm³, causing key-hole porosities for all the investigated compositions.

- A stable key-hole melt pool with a depth between 150 and 250 µm is found for E_d ranging from 80 J/mm³ to 115 J/mm³ for S2, limited to 115 J/mm³ when SiC is added in proportion of 5 or 10% in volume.

- The threshold for the change from conductive to key-hole like melt pool is shifted from E_d of 80 J/mm³ for S2 and S2 + 5% SiC to E_d of 115 J/mm³ for S2 + 10% SiC.

Acknowledgments

References

[1] J. Platl, H. Leitner, C. Turk, A. G. Demir, B. Previtali, R. Schnitzer, Defects in a Laser Powder Bed Fused Tool Steel, Adv. Eng. Mater. 23 (2021) 1-11. https://doi.org/10.1002/adem.202000833

[2] A. Lüddecke, O. Pannitz, H. Zetzener, J. T. Sehrt, A. Kwade, Powder properties and flowability measurements of tailored nanocomposites for powder bed fusion applications, Mater. Des. 202 (2021). https://doi.org/10.1016/j.matdes.2021.109536

[3] J. Wang, R. Zhu, Y. Liu, L. Zhang, Understanding melt pool characteristics in laser powder bed fusion: An overview of single- and multi-track melt pools for process optimization, Adv. Powder Mater. 2 (2023). https://doi.org/10.1016/j.apmate.2023.100137

[4] W. E. King et al., Observation of keyhole-mode laser melting in laser powder-bed fusion additive manufacturing, J. Mater. Process. Technol. 214 (2014) 2915–2925. https://doi.org/10.1016/j.jmatprotec.2014.06.005

[5] E. Gärtner et al., Melt pool signatures of TiN nanoparticle dry-coated Co25Cr25Fe25Ni25 metal powder in laser-powder-bed-fusion, Mater. Des. 226 (2023). https://doi.org/10.1016/j.matdes.2023.111626

[6] S. Zhang, B. Lane, J. Whiting, K. Chou, On thermal properties of metallic powder in laser powder bed fusion additive manufacturing, J. Manuf. Process. 47 (2019) 382-392. https://doi.org/10.1016/j.jmapro.2019.09.012

[7] M. Khorasani et al., The effect of absorption ratio on meltpool features in laser-based powder bed fusion of IN718, Opt. Laser Technol. 153 (2022) 18263. https://doi.org/10.1016/j.optlastec.2022.108263

[8] Z. Zhang et al., 3-Dimensional heat transfer modeling for laser powder-bed fusion additive manufacturing with volumetric heat sources based on varied thermal conductivity and absorptivity, Opt. Laser Technol. 109 (2019) 297-312. https://doi.org/10.1016/j.optlastec.2018.08.012

[9] B. Brandau, A. Da Silva, C. Wilsnack, F. Brueckner, A. F. H. Kaplan, Absorbance study of powder conditions for laser additive manufacturing, Mater. Des. 216 (2022) 110591. https://doi.org/10.1016/j.matdes.2022.110591

[10] O. Pannitz, A. Lüddecke, A. Kwade, J. T. Sehrt, Investigation of the in situ thermal conductivity and absorption behavior of nanocomposite powder materials in laser powder bed fusion processes, Mater. Des. 201 (2021). https://doi.org/10.1016/j.matdes.2021.109530

[11] O. Pannitz, F. Großwendt, A. Lüddecke, A. Kwade, A. Röttger, J. T. Sehrt, Improved process efficiency in laser-based powder bed fusion of nanoparticle coated maraging tool steel powder, Materials (Basel) 14 (2021) 1-22. https://doi.org/10.3390/ma14133465

[12] C. Tan, J. Zou, D. Wang, W. Ma, K. Zhou, Duplex strengthening via SiC addition and in-situ precipitation in additively manufactured composite materials, Compos. Part B Eng. 236 (2022) 109820. https://doi.org/10.1016/j.compositesb.2022.109820

[13] M. H. Mosallanejad, B. Niroumand, A. Aversa, A. Saboori, In-situ alloying in laser-based additive manufacturing processes: A critical review, J. Alloys Compd. 872 (2021) 159567. https://doi.org/10.1016/j.jallcom.2021.159567

[14] E. Saggionetto, E. Filippi, O. Dedry, J. T. Tchuindjang, and A. Mertens, Development and processability of AISI S2 tool steel by laser powder bed fusion, Mater. Res. Proc. 28 (2023) 41-48. https://doi.org/10.21741/9781644902479-5

Numerical modeling of the compressive behavior of 316L body-centered cubic lattice structures

RÍOS Ignacio[1,2,a], MARTÍNEZ Alex[1,b], SAGGIONETTO Enrico[3,c], MERTENS Anne[3,d], DUCHÊNE Laurent[4,e], HABRAKEN Anne Marie[4,f], TUNINETTI Víctor[1,*,g]

[1]Department of Mechanical Engineering, Universidad de La Frontera, Temuco, Chile

[2]Master in Engineering Sciences, Universidad de La Frontera, Temuco, Chile

[3]Department A&M-MMS, University of Liège, Liège, Belgium

[4]Department ArGEnCo-MSM, University of Liège, Liège, Belgium

[a]ignacio.rios@ufrontera.cl, [b]a.martinez16@ufromail.cl, [c]enrico.saggionetto@uliege.be, [d]anne.mertens@uliege.be, [e]l.duchene@uliege.be, [f]anne.habraken@uliege.be, [g]victor.tuninetti@ufrontera.cl

Keywords: Lattice Structure, Additive Manufacturing, Relative Density

Abstract. With additive manufacturing, innovative porous structures emerge for generating lightweight components with high mechanical responses. Body-centered cubic lattice structures are the focus of this study, with customizable lattice density depending on the strut diameter. To predict the properties of lattice structures and thus reduce the number of tests in experimental campaigns, several numerical and analytical models have been developed. In this work, the elastoplastic response was determined. Buckling phenomena of vertical struts depend on the different boundary conditions applied in Finite Element simulations. As shown the number of cells within the model affects the results. This size effect was quantified for different lattice density cases. The numerical results obtained for lattice structures with different relative density were also compared with the well-known Gibson-Ashby model.

Introduction

The development of additive manufacturing technologies and their fabrication capacities has enabled the production of parts with complex three dimensional geometries. These capabilities allow producing parts with innovative designs [1], optimized functionalities [2] and lightweight structures [3] while reducing production cost. Indeed, this process decreases material consumption, production time and post-processing. The lattice structures belong to the complex components built by additive manufacturing.

Lattice structures are based on a cellular representative unit, which is repeated in an orderly fashion in a three-dimensional space. The basic cells – generally called struts-based cells – are defined by constituent rods, with particular geometric dimensions and connectivity at certain points in space called nodes, thus defining their topology. From a cellular point of view, lattice structures can be considered indeed as local structures [4], but from a more macroscopic point of view, they can be considered as a homogenized meta-material distributed in a three-dimensional space with its own mechanical properties [5].

One of the main features of lattice structures is that their global mechanical response can be altered by modifying their topology or geometry parameters such as relative density, cell topology, cell size, among other design parameters. Depending on its design, the lattice structure leads to mechanical properties that significantly differ from those of the constituent material [6].

Cellular structures have been used in several applications, such as aerospace [7], automotive [8], marine [9] and medical [10] industries, owing to the lightweight nature, high strength-to-weight ratio, potential for customization and specific energy absorption capacity [11, 12].

On the basis of the mechanical response, lattice structures can be categorized into bending-dominated or stretch-dominated. Bending-dominated lattice structures experience mostly internal bending moments and are therefore compliant, while stretch-dominated lattice structures experience mainly internal axial loads and are therefore stiffer than bending-dominated structures. In general, the cell topology is the main factor that defines the deformation mechanism of the lattice structure [13].

The most studied strut-based lattice structure topologies are those based on body-centered cubic (BCC), face-centered cubic (FCC) geometries and their variants with reinforcing struts, with the most common one being z reinforcement in the direction of the load (BCCZ and FCCZ). The behavior of these strut-based cells can be characterized by the connectivity of the struts defined in Eq. 1 with the Maxwell number [5, 14], (M). This M-value depends on the number of struts (s) of the representative cell, and the number of nodes, (n).

$$M = s - 3n + 6 \tag{1}$$

For $M < 0$, the system is bending-dominated, while for $M \geq 0$ the structure will display a stretch-dominated behavior. This number is just a general indicator, as the boundary between the two types of behavior is not so clear. It also depends on the orientation of struts versus the load direction.

To decrease the experimental campaigns, many computational models, based on the finite element method, have been developed with the goal of predicting the mechanical behavior of lattice structures, especially those related with the energy absorption capacity of such structures. For instance, Rodrigo et al. [15] presented the quasi-static and dynamic compression behavior of functionally graded lattices by means of experiments and simulations using finite element modeling. The successful validation of their model allowed parametric simulations of the structure subjected to higher compression rates. Wang et al. [13] also investigated the mechanical response and deformation mechanism of a hierarchical lattice structure by means of quasi-static compression tests and numerical simulations. They also found out a good correlation between both methods and proved a superior performance of strut-reinforced hierarchical lattice structures compared to conventional ones. Favre et al. [6] used a continuous crystallographic approach to generate cubic strut-based lattice cells with different topologies and evaluated them through finite element modeling. They found a relationship between the relative elastic modulus and relative density equivalent to the Gibson-Ashby model, with a constant $C = 1$ and an exponent n dependent on the cell topology and geometry.

Computational models have proven to be reliable tools to predict the mechanical behavior of lattice structures, validating analytical models such as the Gibson-Ashby model [16]. However, there is a lack of models evaluating the effect of different boundary conditions in simulations compared with real physical experiments. The present article assesses the impact of the size effect, in terms of number of cells in the studied volume, on the global elastoplastic response of a body centered cubic lattice. The simulations are performed with various boundary conditions and relative densities. They demonstrate the great importance of taking into account the edge effect in lattice structures. Indeed different numbers of cells generate different mechanical responses. The insights and findings reported in this work must be considered when modeling lattice structures as a homogenized material in small domains.